Case study on the ultrafast laser ablation of thin aluminum films: dependence on laser parameters and film thickness

M. Olbrich[1] · E. Punzel[1] · R. Roesch[2,3] · R. Oettking[2,3] · B. Muhsin[2,3] · H. Hoppe[2,3] · A. Horn[1]

Abstract Laser ablation using ultra-short pulsed laser radiation allows the removing of thin films with very high spatial resolution, and working with high repetition rate as well with high through-put. The ultrafast ablation of thin films of aluminum on float glass is investigated using focused femtosecond laser radiation ($\lambda = 1028$ nm, $t_H = 200$ fs, sech^2, $p_f = 1$ MHz) as function of the number of pulses N_p per point (1–10) and the film thickness d (30–300 nm). It is observed that two thresholds are derived simultaneously for thin films with a thickness thicker than 100 nm by irradiating the metal with single pulsed laser radiation exhibiting a Gaussian intensity distribution: one threshold for gentle ablation $H_{thr,gentle}$ and the other for strong ablation $H_{thr,strong}$. Multi-pulse irradiation varying the number of pulses per point identifies the incubation effect described by Jee et al. (J Opt Soc Am B 5(3):648, 1968). This model was applied on the thresholds for gentle and strong ablation. Also, varying the layer thickness reducing the thresholds for thin films due heat accumulation. To quantify the experimental data, numerical simulations solving the coupled heat transfer equation of the two-temperature model were performed. A new approach including the temperature dependence of the reflectivity is presented based on the model proposed by Brückner et al. (J Appl Phys 66:1326, 1989). The results of the simulation fit qualitative well to the experimental data of gentle ablation. Theoretical investigation for double pulses with a variable pulse separation time of 1–300 ps were performed in comparison with a single pulse.

1 Introduction

High-quality micro-structuring of thin metallic films by ultrashort pulsed laser radiation, e.g., no debris, no burr and no damage of the substrate, is of increasing interest for thin film electronics, like organic electronics [3]. In order to describe the removal process consistently, the dependences of the ablation on the laser radiation parameters, e.g., pulse duration, pulse energy, fluence or wavelength, as well as material parameters, like density, reflectivity, heat capacity or heat conductivity, have to be investigated completely. This understanding of ultrashort laser ablation and the change in morphology is also important for the process modeling used in optical metrology, like the ellipsometry, to extract the complex refractive index of the investigated matter being irradiated by laser radiation.

This article is subdivided in five sections. The first section describes the experimental setup and the measurement techniques for determining the experimental data. The next section introduces some theoretical and modeling background. Subsequent, the results for single pulse ablation of thin aluminum films are presented with respect to the obtained ablation regimes as well as the dependency of the ablation threshold on the film thickness. These studies are completed by the results of multi-pulse irradiation, and finally the results are summarized and a short outlook to further work is given.

✉ A. Horn
horn4@hs-mittweida.de

1   Laserinstitut Hochschule Mittweida, Technikumplatz 17, 09648 Mittweida, Germany

2   Institute of Organic and Macromolecular Chemistry, Friedrich-Schiller-Universität Jena, Humboldtstr. 10, 07743 Jena, Germany

3   Center for Energy and Environmental Chemistry Jena (CEEC Jena), Friedrich-Schiller-Universität Jena, Philosophenweg 7a, 07743 Jena, Germany

2 Experimental setup and measurement

The laser radiation, provided by a femtosecond laser system (Pharos, Light Conversion Ltd., $\lambda = 1028$ nm, $\tau_H = 200$ fs, $M^2 = 1.2$), is guided by high-reflecting dielectric mirrors to the focusing setup. An internal Pockels-cell allows to deliver single pulses, or pulse bursts with defined number of pulses at defined pulse repetition rate, here $f_p = 1$ MHz. The laser radiation is positioned on the target surface by a X–Y-galvanometer scanner (intelliSCANde, Scanlab AG) mounted on a motorized linear stage, and is focused on the target surface ($d_\sigma = 30$ μm) using a f-Θ-objective ($f = 167$ mm). The investigated aluminum films were deposited by sputtering on float glass. The roughness of the surface and the crystallinity were not measured. For sake of simplicity, the thermo-physical and optical properties are assumed to be the properties of bulk aluminum. The surface topology of the ablation structures was investigated by optical microscopy (Nikon Labophot-2 in transmission and reflection mode) and by confocal microscopy (Confovis GmbH).

3 Fundamentals and modeling

The laser radiation reaching the surface of a material is partially reflected or transmitted according to the Fresnel equations [4] and afterward absorbed within the material by the electron system depending on the absorption coefficient. Thereby, the electron system is excited into a non-equilibrium state [5]. The electrons collide with each other and transfer energy. After a defined time, called relaxation time τ_{rel}, a thermal equilibrium within the electron system is reached and the energy distribution of the electron system can be described by a Fermi distribution. Assuming that these relaxation time τ_{rel} is small compared to the pulse duration τ_H, the energy transfer between the electron and the phonon systems can be described by the two-temperature model (TTM) proposed by [6] and expanded by many authors like [5, 7]. The heat conduction equation for the electron system is given by

$$C_{e_V}(T_e) \cdot \frac{\partial T_e}{\partial t} = \nabla \cdot \left(\lambda_{th_e}(T_e, T_{ph}) \cdot \nabla T_e \right) - G(T_e) \cdot (T_e - T_{ph}) + q_V(\mathbf{r}, t), \qquad (1)$$

and the heat conduction equation for the phonon system by

$$C_{ph_V} \cdot \frac{\partial T_{ph}}{\partial t} = G(T_e) \cdot (T_e - T_{ph}). \qquad (2)$$

The volumetric heat capacity of the electrons $C_{e_V}(T_e)$ and the coupling factor $G(T_e)$ were taken from [8]. The thermal conductivity of the electrons λ_{th_e} is described by the Drude model according to

$$\lambda_{th_e}(T_e, T_{ph}) = \frac{1}{3} \cdot v_F^2 \cdot C_{e_V}(T_e) \cdot \tau_e(T_e, T_{ph}). \qquad (3)$$

v_F represents the Fermi velocity and is assumed to be constant. q_V represents the volumetric heat source, and τ_e the relaxation time of the electrons, which is the time among two impacts between two electron or one electron and one phonon. The volumetric heat source is given by

$$q_V(\mathbf{r}, t) = I_0 \cdot \left(\frac{w_0}{w(z_S - z_0)} \right)^2 \cdot \alpha(z_S)$$
$$\cdot (1 - R(z_S)) \cdot e^{-\int_{z_S}^{z} \alpha(r,z)d\zeta}$$
$$\cdot e^{-2 \frac{r^2}{w^2(z_S - z_0)}} \cdot \text{sech}^2 \left(1.763 \cdot \frac{t - t_0}{\tau_H} \right). \qquad (4)$$

$z_S = z_S(r)$ represents the position of the surface depending on the lateral position, I_0 the maximum intensity at the waist position z_0 given by $I_0 = \frac{2 \cdot Q}{\pi \cdot w_0^2 \cdot 1.1344 \cdot \tau_H}$, w_0 the waist radius at z_0, w the beam radius at z_S, $R(z_S)$ the reflectivity on the surface, t_0 the maximum peak time, Q the pulse energy and α the absorption coefficient. α can be expanded to include the range of ballistic electrons as described by [5], but in our formula the absorption coefficient is only described by the complex refractive index. For the simulations, the initial position of the surface is equal to the position of the beam waist and is set to zero, so $z_0 = z_S = 0$. If vaporization occurs, z_S changes. An expansion of the material due to heating is neglected. All following calculations are related to aluminum. The relaxation time τ_e can be calculated by [9, 10]

$$\frac{1}{\tau_e} = A_e \cdot T_e^2 + B_{ph} \cdot T_{ph}. \qquad (5)$$

The Parameter A_e was derived from [10] to $0.376 \cdot 10^7 \frac{1}{\text{s} \cdot \text{K}^2}$ and the commonly used value for the parameter B_{ph} is $3.9 \cdot 10^{11} \text{s}^{-1} \text{K}^{-1}$ [10]. As a new proposal, now the parameter B_{ph} will be directly coupled to the experimental data. Assuming that the temperature of the electron system equals to the temperature of the phonon system, τ_e is only determined by the phonon system $\frac{1}{\tau_e} \approx B_{ph} \cdot T_{ph}$. This relaxation time is also used in the Drude model calculating the relative permittivity for intraband processes $\tilde{\varepsilon}_{r,intra}$ [2, 11]

$$\tilde{\varepsilon}_{(r,intra)} = 1 - \frac{\sigma_0 \cdot \tau_e}{\varepsilon_0 \cdot (1 + \omega^2 \cdot \tau_e^2)} - i \cdot \frac{\sigma_0 \cdot \tau_e}{\varepsilon_0 \cdot \omega \cdot (1 + \omega^2 \cdot \tau_e^2)} \qquad (6)$$

where σ_0 represents the dc conductivity, ε_0 the vacuum permittivity, and ω the frequency of the laser radiation. Equation (6) is also often written in terms of the plasma-frequency $\omega_p = \frac{n_e \cdot e^2}{\varepsilon_0 \cdot m_e}$, e.g., in [11, 12]. These formulas are equal and can be converted into each other. The relaxation time can also be determined by

$$\tau_{e}(T) = \frac{\sigma_0(T) \cdot m^*}{e^2 \cdot n_e(T)}, \tag{7}$$

where e represents the elementary charge, n_e the density of conduction electrons, and m^* the effective mass of the electrons [2]. Here, to include effects of the lattice potential, the effective mass is used instead of the classical electron mass. All parameters on the right side of Eq. (7), except e, are temperature dependent. The parameters $\sigma_0(T)$ for the solid and liquid state of aluminum are derived from [13]. For the solid state, m^* can be obtained comparing the experimental and theoretical value of the Sommerfeld-parameter γ and is tabulated in [14]. The value of m^* for the liquid state was taken from [2]. The density of the conduction electrons n_e can be derived by the change of density $\rho(T)$ [15] according to

$$n_e(T) = v \cdot \frac{\rho(T)}{m_A}, \tag{8}$$

where v represents the number of valence electrons and m_A the atomic mass. Under equilibrium conditions the relaxation time is only determined by the phonon system, and one can combine Eqs. (5), (7) and (8) to

$$B_{ph}(T_{ph}) = \frac{e^2}{\sigma_0(T_{ph}) \cdot m^* \cdot T_{ph}} \cdot v \cdot \frac{\rho(T_{ph})}{m_A}. \tag{9}$$

Another method for calculating B_{ph} is based on the measured temperature-dependent values of the thermal conductivity $\lambda_{th_0}(T)$. The necessary values are derived from [16]. The values for $\lambda_{th_0}(T)$ include the contribution of the electron (λ_{th_e}) and phonon ($\lambda_{th_{ph}}$) system. Assuming again equal temperatures of both systems, the thermal conductivity is purely determined by the electron system [17], $\lambda_{th_e} \gg \lambda_{th_{ph}}$, but depending on the phonon temperature. Applying Eqs. (3) and (5) for a thermal equilibrium gets

$$B_{ph}(T_{ph}) = \frac{v_F^2 \cdot C_{ev}(T_{ph})}{3 \cdot \lambda_{th_0}(T_{ph}) \cdot T_{ph}}. \tag{10}$$

The comparison between the commonly used value for B_{ph} in literature and the value derived with Eqs. (9) and (10) are visualized in Fig. 1. Applying the average of Eqs. (9) and (10) at room temperature results in the value used in literature and was also confirmed for the metals gold, silver and copper. Therefore, the average is used for the following calculations.

The finally resulting thermal conductivity of the electrons λ_{th_e}, according to Eq. (3) and including Eqs. (5), (9) and (10), are depicted in Fig. 2 for different temperatures of the electron and phonon system.

Vice versa, Eq. (5) leads for different temperatures of the electron and phonon system to a temperature-dependent permittivity $\tilde{\varepsilon}_r(T_e, T_{ph})$. This approach is an extension of a
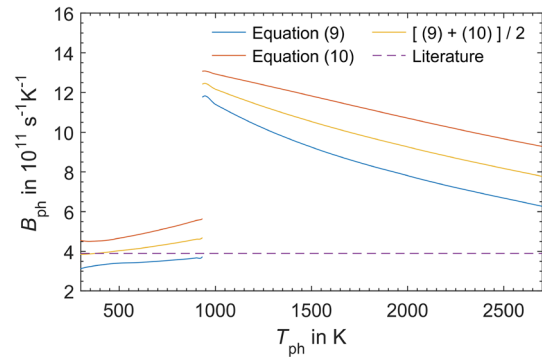

Fig. 1 Dependence of the parameter B_{ph} on the phonon temperature in comparison with the used value in literature (*dashed line*)
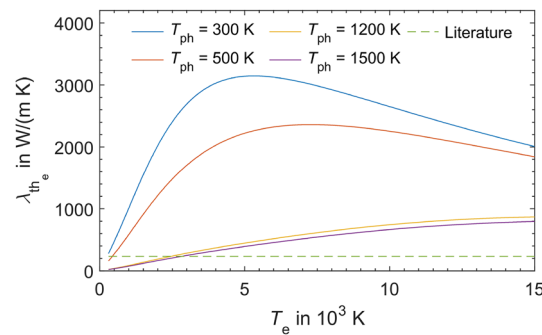

Fig. 2 Dependence of the thermal conductivity of the electrons on the electron temperature for four different phonon temperatures in comparison with the thermal conductivity of aluminum at room temperature (*dashed line*)

proposed model by [2] considering the temperature dependence of reflectivity using Eq. (7). Instead of Eqs. (7), (5) can be used with the average of Eqs. (9) and (10). The total permittivity includes also the interband effects, which can be described by the Lorentz model

$$\tilde{\varepsilon}_r = \tilde{\varepsilon}_{r,intra} + \tilde{\varepsilon}_{r,inter},$$

$$\tilde{\varepsilon}_r = \tilde{\varepsilon}_{r,intra} + \sum_{j=1}^{N} \frac{f_j \cdot \omega_p^2}{\omega_j^2 - \omega^2 + i \cdot \Gamma_j \cdot \omega}. \tag{11}$$

f_j represents the weight of the j-th oscillator with the frequency ω_j, and Γ_j the damping constant, where $\tau_j = 1/\Gamma_j$ represents the lifetime [11]. The complex permittivity refers to the refractive index by

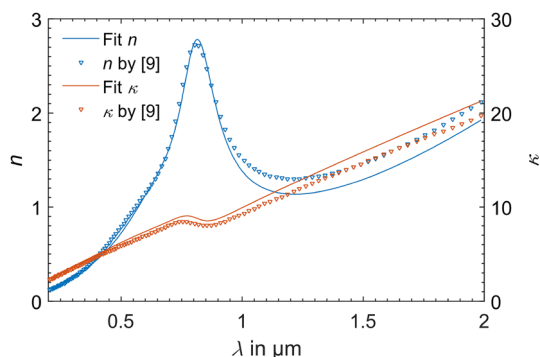$$\tilde{n} = \sqrt{\tilde{\varepsilon}_r} = n - i \cdot \kappa. \tag{12}$$

All parameters of the interband contributions are also temperature dependent, but the only known dependency is again given by the density of conduction electrons, Eq. (8), in ω_p. The other parameters are set constant. As all parameters in the Lorentz model, including the intraband contribution $\tilde{\varepsilon}_{r,intra}$, are fitted to experimental data [11], the fit has to be repeated and set the intraband contribution

$\tilde{\varepsilon}_{r,\text{intra}}$ to constant. The final result of n and κ can be seen in Fig. 3. The approximated function fits well to the experimental data for small wavelength, but has a difference for larger wavelengths beginning at about 1 μm. This difference is used as a constant offset in all simulations. It should be noted that the effects of the temperature-dependent interband contribution are small compared to the temperature-dependent intraband part.

Based on the calculated complex refractive index, the reflectivity R for perpendicular incidence [4] and for the transition air to metal, is given as function of electron temperature for different phonon temperatures (Fig. 4).

All simulations are performed for two-dimensional axial symmetry. Equations (1) and (2) are discretized by Finite Differences and solved by a convolution of the temperature distribution and a convolution kernel for the derivatives, as it is state of the art in digital image processing. The numerical change of the phase state is based on a formula used by [18] considering the latent heat of fusion ΔH_M and of vaporization ΔH_V in the volumetric heat capacity of the phonons.

$$C_{\text{ph}_V} = \rho(T_{\text{ph}}) \cdot \left[c_{p_0} + \frac{\Delta H_{\text{M}}}{\Delta T \cdot \sqrt{2 \cdot \pi}} \cdot e^{-\frac{1}{2}\left(\frac{T_{\text{ph}} - T_{\text{M}}}{\Delta T}\right)^2} \right.$$
$$\left. + \frac{\Delta H_{\text{V}}}{\Delta T \cdot \sqrt{2 \cdot \pi}} \cdot e^{-\frac{1}{2}\left(\frac{T_{\text{ph}} - T_{\text{V}}}{\Delta T}\right)^2} \right]. \qquad (13)$$

Fig. 3 Comparison of the experimental data of n and κ [10] to the fit of the Lorentz model as a function of the wavelength
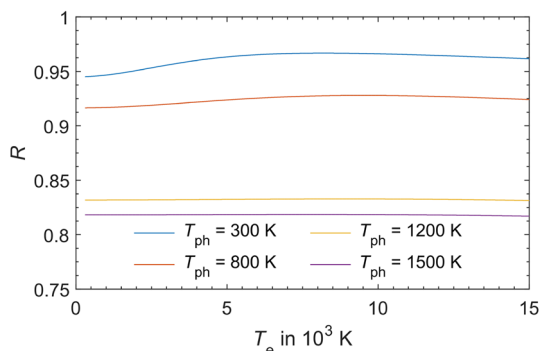

Fig. 4 Dependence of the reflectivity on the electron temperature for four different phonon temperatures

c_{p_0} represents the heat capacity calculated by the Debye model [14] and set to be constant. The parameter ΔT determines the width of the zone of phase change and should be 20 K up to 50 K. T_{M} and T_{V} are the melting and vaporization temperature, respectively. If the phonon temperature of a pixel rises $T_{\text{M}} + \Delta T/2$, it is considered as melted. Similar, if the phonon temperature of a pixel rises $T_{\text{V}} + \Delta T/2$, it is considered as vaporized, and excluded from the simulations.

One example, describing heating a 300 nm thick aluminum film irradiating it by three different pulse energies using the experimental parameters, as well as all described fundamentals, is visualized in Fig. 5.

The reflectivity decreases during irradiation leading to increased absorbed energy and higher electron temperatures (Fig. 5). Increasing the pulse energy decreases the time to reach a minimum reflectivity given by the absorbed energy and increases the reached maximum phonon temperature. Therefore, for higher pule energies, more energy is absorbed during the laser pulse. In contrast to the simulations, higher pulse energies in the experiment lead not necessarily to more ablated volume, because some limiting processes, like interaction of the laser radiation with the ablated particles and the evolution of a plasma, occur. A jump in reflectivity during the phase transition from liquid to vapor can also be identified. Larger pulse energies lead to higher electron temperatures, and the relaxation time τ_{R} to reach a thermal equilibrium between the electron and phonon system, increases too. This is in agreement to the theory as the relaxation time $\tau_{\text{R}} = C_{\text{ev}}/G$ increases with higher electron temperatures for aluminum [8]. Furthermore, the phonon temperature increases faster for higher
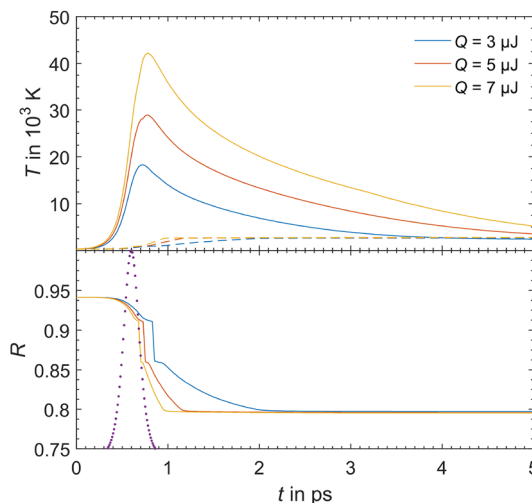

Fig. 5 Simulation results for three different pulse energies; *solid lines* maximum electron temperature T_{e}; *dashed lines* maximum phonon temperature T_{ph}; points: temporal power distribution in a.u.; peak power at $t_0 = 600$ fs

pulse energies compared to lower pulse energies justified by the high temperature difference $T_e - T_{ph}$.

4 Single-pulse ablation

Several thin films of aluminum were irradiated by focused femtosecond laser radiation. Three different topologies of the resulting structures were observed (Fig. 6). For a film thickness of $d = 300$ nm, an outer (gentle ablation) and an inner diameter (strong ablation) of the ablation structure was formed by the laser radiation. Plotting the measured ablation depth z_A by confocal microscopy as function of the peak fluence $H_0 = \frac{2 \cdot Q}{\pi \cdot w^2}$ two regimes can be distinguished by the different obtained ablation depths (Fig. 7). For thin films, like $d = 100$ nm, just one topology is visible representing an overlap of both regimes. For thin films with a thickness between 100 and 300 nm, a differentiation between the two regimes can be detected. Films with a thickness of 150 nm represent a transition regime, because the separation begins and no clear differentiation is possible. Therefore, the outer structures are assigned to the gentle ablation and the inner diameter to the strong ablation.
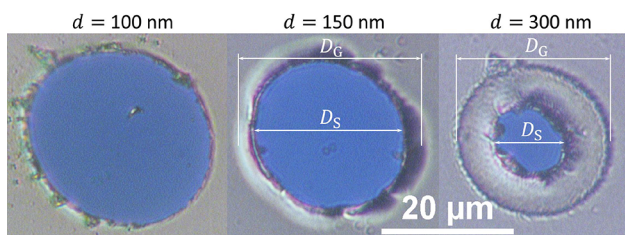
Fig. 6 Ablation structures for three different film thicknesses irradiated with the same pulse energy of $Q = 7\,\mu$ J; *blue* float glass substrate; detected by optical microscopy, D_S-diameter strong ablation, D_G-diameter gentle ablation
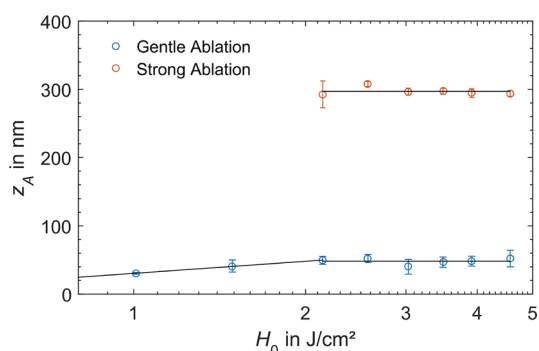
Fig. 7 Single-pulse ablation depths z_A as a function of the fluence; $d = 300$ nm; detected by confocal microscopy, fit to guide the eye

For a film thickness of 300 nm and using low peak fluences up to 2.2 J/cm², only gentle ablation occurs and a small increase in the ablation depth z_A can be detected for increasing fluence (Fig. 7). Beginning from a peak fluence of 2.2 J/cm² the regime for strong ablation can be detected and an ablation depth independent of the peak fluence for gentle ablation is measured. In the strong ablation regime, the metal film is completely removed. An analytical description of the ablation depth for the two ablation regimes as a function of the fluence can be found in [7, 19] predicting a logarithmic dependency of the ablation depth on the fluence for gentle ablation and a linear dependency for strong ablation. This is in contrast to other authors, like [20, 21], applying a logarithmic dependency for strong ablation, too. Nevertheless, all of these formulas are not applicable for our experiments, because our film thicknesses are too small and the complete film is ablated with one pulse. Therefore, for strong ablation, no linear or logarithmic dependency on the fluence can be stated. Furthermore, the threshold for occurring of strong ablation can not be explained by the formulas used by [20, 21].

Recasts of melting could be observed on the border of the ablation structures, like ejections and ring-like structures (Fig. 6), indicating an explosion process of molten material often discussed in literature, such as coulomb explosion for gentle ablation [22], and phase explosion [22, 23] as well as critical-point phase separation [24] for strong ablation. Furthermore, the results support the model proposed by [25] of forming bumps and jets or droplets. The numerical investigations of [26] identifies thermal stress caused by ultrafast heating and melting as the driving mechanism for forming bumps, but the authors only concentrated on irradiating the thin film from the glass substrate back side.

The diameters D of the ablation structures were measured by optical microscopy, and in a first step the squared diameter, for the strong and gentle regime, over the log pulse energy was applied for determination of the beam radius w and the threshold pulse energy Q_{thr}. Based on the results, the threshold fluence $H_{thr} = \frac{2 \cdot Q_{thr}}{\pi \cdot w^2}$ can be derived. In the second step the diameter squared over log peak fluence H_0 is performed (Fig. 8). The determined beam radius w of the gentle ablation measurements is also used for strong ablation, as the same laser beam creates both ablation structures.

The derived thresholds fluences are summarized in Fig. 9 and compared with the simulated thresholds at the same laser parameters.

For thin layers $d < 100$ nm, smaller thresholds due to heat accumulation (Fig. 10) were obtained experimentally and by simulation. The reason is just a 2D heat diffusion to surrounding areas instead of a 3D diffusion. It can also be
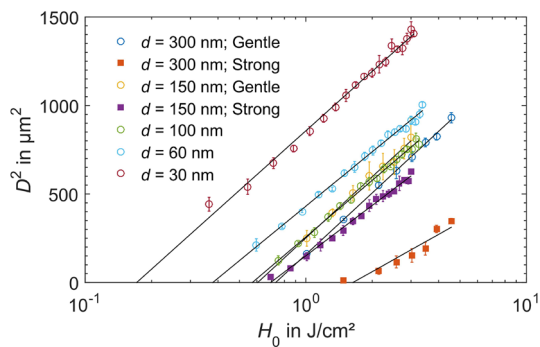
Fig. 8 Squared diameter over log peak fluence for different thin film thicknesses of aluminum
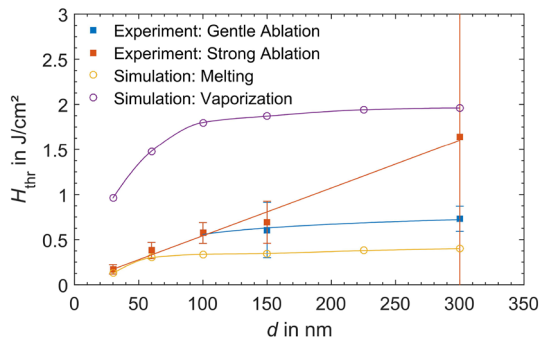
Fig. 9 Experimentally and by simulation derived thresholds of gentle and strong ablation in dependence of the layer thickness, all lines to guide the eye

observed that the separation in gentle and strong ablation regime, beginning from just one regime, starts at 100-nm film thickness. For strong ablation an approximately linear dependency on the film thickness was detected, whereas the gentle ablation regime converges against an upper limit for bulk material [6]. The error bars for strong ablation and $d = 300$ nm are very large due to less data points and high fluctuations of the detected diameters; therefore, a logarithmic dependency of the ablation threshold on the film thickness, as for gentle ablation, cannot be excluded. A linear dependency of the ablation threshold on the film thickness for removing thin aluminum films with a single pulse was reported by [28] corresponding to our experiments on strong ablation. In contrast to our determined thresholds, the authors of [28] reported much larger fluences using a different measurement technique for threshold determination, detecting the LIBS-signal (laser induced breakdown spectroscopy) of the substrate. A qualitative agreement of the simulated melting thresholds with the experimental ablation thresholds for gentle ablation let us assume a non-thermal explosion as the dominating ablation process for this ablation regime (Fig. 9). Numerical investigations of [29, 30] describing lifting of a small liquid layer up from the surface, although no vaporization occurs,
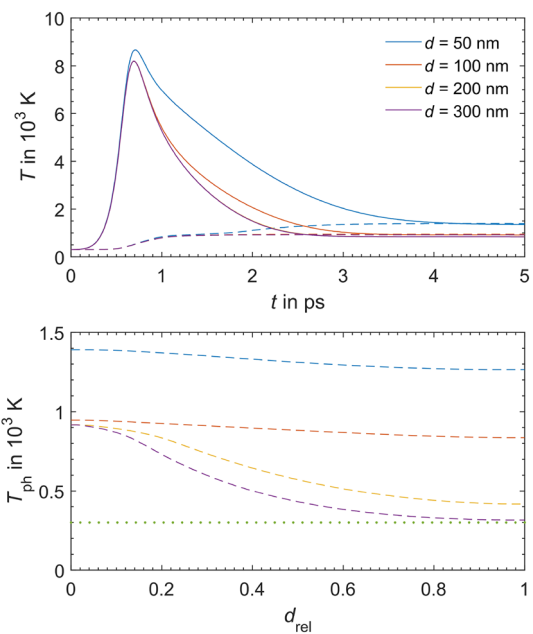

Fig. 10 Simulated temperature distribution for four different film thicknesses of aluminum by irradiating with a single pulse ($Q = 1$ μJ); *Top* Temperature as function of time, maximum electron temperature (*solid lines*), maximum phonon temperature (*dashed lines*); *Bottom* Phonon temperature as function of normalized film thickness (*dashed lines*) at $t = 5$ ps compared with room temperature (*dotted line*)

supports our assumption. In contrast, an agreement of the simulated threshold for vaporization to strong ablation is not possible. Nevertheless, the simulated results show the need of including a temperature-dependent reflectivity, because without, no vaporization can be derived.

The simulations depict clearly a higher phonon temperature for smaller film thicknesses due to heat accumulation (Fig. 10 bottom). In contrast to thin films, where the film is nearly homogeneously heated, the bottom end of the film for $d = 300$ nm remains cold. Furthermore, the highest electron temperature for very small film thicknesses $d = 50$ nm is reached, and the time for reaching the thermal equilibrium between electron and phonon system last longest, since heat accumulation takes also in the electron system place. Due to higher temperatures at the same pulse energy, the ablation threshold for thin films gets smaller than for thicker ones. This trend is also confirmed for $d = 50$ nm as melting occurs ($T_{ph} > T_M$; $T_M = 933$ K) and the other films stay in the solid state.

5 Multi-pulse ablation

A distinct separation between gentle and strong ablation was only clearly observed for the film thickness $d = 300$ nm. Thus, only the ablation thresholds for
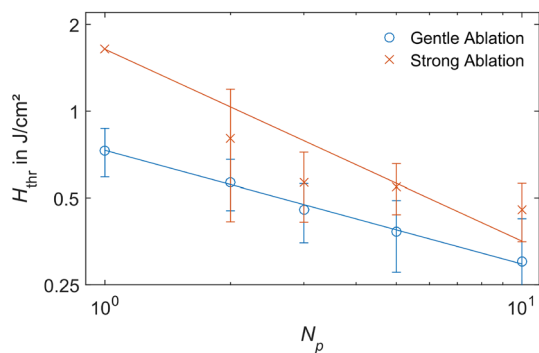
Fig. 11 Dependence of the experimentally derived thresholds for gentle and strong ablation on the number of pulses per point for a layer thickness $d = 300$ nm; Fit for calculation of incubation parameter S
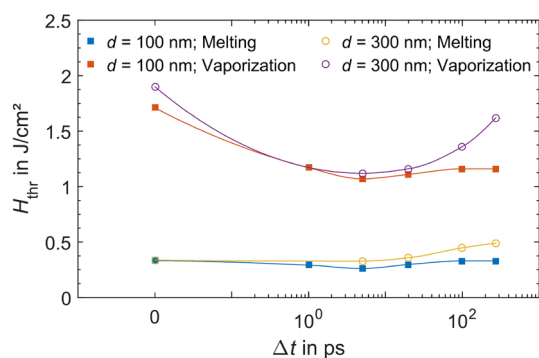
Fig. 12 Simulated thresholds for melting and vaporization as a function of the pulse separation time compared with a single pulse (separation time zero)

$d = 300$ nm are presented (Fig. 11). The applied fluence is only based on the fluence of the single pulse and not on the sum of the pulse energy of all pulses.

An increasing number of pulses per point leads to a reducing of the thresholds. This dependence of the threshold can be led back on an incubation effect described by the incubation model of Jee [1]

$$H_{\text{thr}}(N_{\text{p}}) = H_{\text{thr}}(1) \cdot N_{\text{p}}^{S-1}, \tag{14}$$

with the fitting parameters $S_{\text{gentle}} = 0.606$ and $S_{\text{strong}} = 0.336$.

For these experiments, no comparison simulations were performed for the large pulse separation time of 1 μs, given by the setup, leading to very long computation times. Therefore, some theoretical simulations for double pulses with a variable pulse separation time from 1 up to 300 ps were performed for a layer thickness of 100–300 nm (Fig. 12). The results for the double pulses are compared with a single pulse having the same pulse energy as the sum of the pulse energy of the two double pulses. Also, the threshold fluence is calculated by the sum of the pulse energy.

A minimum of the thresholds for melting and vaporization at about 5–10 ps is observed (Fig. 12) resulting from a minimum of the reflectivity at this time. This time represents nearly the relaxation time τ_{R}. For longer separation times, the diffusion of heat to the surrounding areas lead to smaller electron and phonon temperatures and the reflectivity increases. Furthermore, for shorter separation times, the phonon temperature reaches its maximum and according to Fig. 4 the reflectivity reaches its minimum. A distinct minimum of the threshold fluence for vaporization is determined for $d = 300$ nm. For $d = 100$ nm the thresholds for melting and vaporization converge against a limit smaller than the thresholds for single pulses resulting from the heat accumulation. Therefore, the thresholds for $d = 100$ nm are also smaller than the thresholds for $d = 300$ nm. No comparable results for aluminum were found in literature as mostly only the ablation depth is the subject of investigations [31, 32].

6 Summary and outlook

The thresholds for single-pulse ablation were determined by applying the squared diameter over log peak fluence. Two ablation regimes, the gentle and the strong ablation, were classified for layer thicknesses $d > 100$ nm. For smaller film thicknesses just one ablation regime could be determined. As a result, smaller thresholds were obtained by reducing the layer thickness due to heat accumulation. The threshold for strong ablations features a linear dependence on the film thickness. For further investigations to this dependency, experiments with thicker films and higher fluences are necessary. A qualitative agreement between the experiments for single pulses and the irradiation in the gentle ablation regime with the simulated melting thresholds could be achieved. Recasts of melting could be detected around the ablation structures of the two ablation regimes indicating explosive processes, such as coulomb, phase explosion, critical-point phase separation or thermal stress due to ultrafast heating as the dominant ablation processes.

The simulation can not discriminate the two experimentally observed ablations regimes. So, further models have to contain other ablation mechanisms, like phase explosions. To predict the observed ablation structures, a coupling with beam propagation is also necessary.

An increasing number of pulses per point led to a reducing of the thresholds described by incubation model of Jee. Due to the long computation times for a pulse separation time of 1 μ s, theoretical investigations performed for double pulses with a separation time between 1 and 300 ps describe a minimum for the thresholds of melting and vaporization at about 5–10 ps.

References

1. Y. Jee, M.F. Becker, R.M. Walser, J. Opt. Soc. Am. B **5**(3), 648 (1988)
2. M. Brückner, J.H. Schäfer, J. Uhlenbusch, J. Appl. Phys. **66**, 1326 (1989)
3. S. Logothetidis, *Handbook of Flexible Organic Electronics. Materials, Manufacturing and Applications* (Elsevier, Amsterdam, 2015)
4. M. Born, E. Wolf, A.B. Bhatia, *Principles of Optics. Electromagnetic Theory of Propagation, Interference and Diffraction of Light* (Cambridge University Press, Cambridge, 2013)
5. S.-S. Wellershoff, J. Hohlfeld, J. Güdde, E. Matthias, Appl. Phys. A **69**(S1), 99–107 (1999)
6. S.I. Anisimov, B.L. Kapeliovich, T.L. Perel'man, JETP **39**, 375 (1974)
7. B.H. Christensen, K. Vestentoft, P. Balling, Appl. Surf. Sci. **253**(15), 6347–6352 (2007)
8. Z. Lin, L.V. Zhigilei, V. Celli, Phys. Rev. B **77**(7), 075133 (2008)
9. X.Y. Wang, D.M. Riffe, Y.-S. Lee, M.C. Downer, Phys. Rev. B **50**(11), 8016–8019 (1994)
10. F. Chen, G. Du, Q. Yang, J. Si, H. Hou, in *Two Phase Flow, Phase Change and Numerical Modeling*, ed. by A. Ahsan (InTech, Winchester, 2011)
11. A.D. Rakic, A.B. Djurišic, J.M. Elazar, M.L. Majewski, Appl. Opt. **37**(22), 5271 (1998)
12. J. Hohlfeld, D. Grosenick, U. Conrad, E. Matthias, Appl. Phys. A **60**(2), 137–142 (1995)
13. P.D. Desai, H.M. James, C.Y. Ho, J. Phys. Chem. Ref. Data **13**(4), 1131 (1984)
14. C. Kittel, *Introduction to Solid State Physics* (Wiley, Hoboken, 2005)
15. W.M. Haynes, D.R. Lide, *CRC Handbook of Chemistry and Physics* (CRC Press, Boca Raton, 2012)
16. R.W. Powell, C.Y. Ho, P.E. Liley, *Thermal Conductivity of Selected Materials* (U.S. Dept. of Commerce, National Bureau of Standards, Washington, 1966)
17. Wellershoff, S.-S. Untersuchungen zur Energierelaxationsdynamik in Metallen nach Anregung mit ultrakurzen Laserpulsen. Ph.D. thesis, Berlin (2000)
18. J. Sotrop, M. Domke, A. Kersch, H.P. Huber, Phys. Procedia **41**, 520–523 (2013)
19. Byskov-Nielsen, J., Short-pulse laser ablation of metals: fundamentals and applications for micro-mechanical interlocking. Ph.D. thesis (2010)
20. X. Zhao, Y.C. Shin, Appl. Surf. Sci. **283**, 9499 (2013)
21. I. Mingareev, *Ultrafast Dynamics of Melting and Ablation at Large Laser Intensities* (Cuvillier, Göttingen, 2009)
22. E.G. Gamaly, Phys. Rep. **508**(4–5), 91243 (2011)
23. C.R. Phipps, *Laser Ablation and its Applications. Springer Series in Optical Sciences*, vol. 129 (Springer, New York, 2007)
24. B. Wu, Y.C. Shin, Appl. Surf. Sci. **253**, 40794084 (2007)
25. M. Domke, S. Rapp, H.P. Huber, Phys. Procedia **39**, 717–725 (2012)
26. J. Sotrop, A. Kersch, M. Domke, G. Heise, H.P. Huber, Appl. Phys. A **113**, 397–411 (2013)
27. J.M. Liu, Opt. Lett. **7**(5), 196 (1982)
28. B. Le Drogoff, F. Vidal, Y. von Kaenel, M. Chaker, T.W. Johnston, S. Laville, M. Sabsabi, J. Margot, J. Appl. Phys. **89**(12), 8247 (2001)
29. M.E. Povarnitsyn, T.E. Itina, Appl. Phys. A **117**(1), 175–178 (2014)
30. S. Sonntag, J. Roth, F. Gaehler, H.-R. Trebin, Appl. Surf. Sci. **255**(24), 9742–9744 (2009)
31. M.E. Povarnitsyn, T.E. Itina, P.R. Levashov, K.V. Khishchenko, Appl. Surf. Sci. **257**(12), 5168–5171 (2011)
32. A. Semerok, C. Dutouquet, Thin Solid Films **453–454**, 501–505 (2004)